Research Article

Disordered Ferlin C2A–C2B Linkers Bind Membranes and Encode Small Linear Motifs

Ethiene Kwok † **Patricia Khuu** † **Erin Huang, Fakhria Saadat, Elijah Urbaitel, Jordan S. Indrawan, Patrick Reardon, Juan Vanegas, and Colin P. Johnson** *

Department of Biochemistry and Biophysics Oregon State University, *Corvallis, OR, USA*

Correspondence to Colin P. Johnson: Department of Biochemistry and Biophysics, Oregon State University, Corvallis, OR 97333, USA. *colin.johnson@oregonstate.edu (C.P. Johnson)*
https://doi.org/10.1016/j.jmb.2025.169419
Edited by Lutz Schmitt

Abstract

Ferlins are vesicle trafficking proteins composed of folded C2 domains conjugated by linkers which are largely disordered. Although a role for the C2 domains as calcium sensors has been established it remains unclear whether the linkers function beyond acting as passive spacers. We examined the C2A–C2B linker sequences of vertebrate ferlins and found both putative short linear motifs (SLiMs) as well as membrane binding sequences for members of the protein family. Specifically, for otoferlin we identified an arginine-rich region proximal to an AP2 binding dileucine motif which interacts with negatively charged lipid membranes. Further, the linker region dominated the liposome binding properties of a larger recombinant C2A–C2B, two-C2 domain segment of otoferlin, suggesting a dominant role in mediating the membrane binding property of the N-terminus. We also found that alternative splicing of the otoferlin C2A–C2B linker adds an additional membrane binding segment and alters the affinity of membrane binding. Like otoferlin, a recombinant dysferlin linker interacted with liposomes. However, dysferlin encodes for SLiMs not detected in the otoferlin linker and interacted with both SH3- and WW- domain proteins as determined using fluorescence spectroscopy. We conclude that the C2A–C2B linker of vertebrate ferlins serves as a signaling platform by recruiting SLiM-binding partners. Membrane binding "hotspots" encoded in a subset of linkers including otoferlin may serve to localize protein complexes proximal to the cell membrane for activity.

Published by Elsevier Ltd.

Introduction

Intrinsically disordered regions (IDR) are protein sequences which lack a well-defined structure and typically populate a variety of conformations. This enhanced flexibility allows for functions that structured domains cannot easily achieve. For example, IDRs can enhance binding interactions by extending to capture a target protein using a fly-casting mechanism [1]. Alternatively, some vesicle trafficking proteins contain disordered sequences which bind and promote membrane budding [2]. However for many proteins the contribution of the IDR remains uncharacterized. An example is the sensory hair cell protein otoferlin, which resides on synaptic vesicles and contributes to exocytosis and endocytosis at the ribbon synapse [3,4]. Otoferlin consists of multiple folded C2 domains (denoted C2A–C2G) bridged by long intrinsically disordered linkers. While the membrane and Ca^{2+} binding properties of the folded C2 domains have been established, it is unknown whether the IDRs between domains serve a functional role beyond acting as a passive spacer [5,6]. Otoferlin is one of six ferlin genes within mammals, and while the linkers are found in all vertebrate family members, the amino acid sequences differ substantially [7]. Further, alternative splicing

of ferlin linkers have been reported, including otoferlin brain and sensory hair cell isoforms which differ in C2A–C2B linker composition [8]. An otoferlin splice variant lacking the first 182 amino acids including the C2A–C2B linker has also been reported in sensory hair cells [3,8–10]. This shortened variant displayed abnormal endocytic membrane retrieval and a reduced ability to conduct sustained exocytosis [10]. Splicing of the dysferlin C2A–C2B linker has also been reported, which inserts 30 amino acids within the middle of the linker [11,12]. However, although the use of alternative sequences within the linkers suggests functional activity, no study has specifically examined the properties of any ferlin linker. In this study we examine the C2A–C2B linker of vertebrate ferlins using a combination of coarse-grained simulation, recombinant protein assays, and solution NMR.

Materials and Methods

Protein production and purification

pcDNA3.1 otoferlin plasmid (gift from C. Petit, Institute Pasteur et Université Pierre et Marie Curie, France) and pcDNA4/TO/GFP-dysferlin-myc-his (gift from K. Bushby Newcastle, U.K) were used as templates for amplification of Mus Musculus otoferlin (GenBank: AY586513.1) and Homo sapiens dysferlin (GenBank: AF075575.1), respectively. The C2A–C2B linkers were cloned into a pET28a (+) vector (Novagen) between the BamHI and HindIII restriction sites with a TEV sequence inserted between the linker and polyhistidine sequences. Full-length Mus Musculus endophilin A1 was cloned into a pGEX2T vector (GE HEalthcare) with a thrombin sequence between endophilin and the glutathione tag. For linker proteins, BL21-CodonPlus (Agilent) cells containing the expression plasmid were cultured overnight at 37 °C in Luria-Bertani broth containing 1% w/v glucose and 50 μg/mL kanamycin and 25 μg/mL chloramphenicol were used to seed 1-liter cultures of Luria-Bertaini broth with kanamycin. ^{15}N and $^{15}N/^{13}C$ isotopically labeled protein was produced by bacteria grown in MJ9 media containing 1 g/L $^{15}NH4Cl$ and 2 g/L of ^{12}C or ^{13}C glucose. Cultures were grown to an optical density of 0.6 at 37 °C and induced with 0.5 mM isopropyl β-D1-thiogalactopyranoside (IPTG) for 16 h at 18 °C. Cultures were centrifuged at 4000 rpm at 4 °C for 20 min and resuspended in lysis buffer: 50 mM HEPES pH 8, 250 mM NaCl, 10% (v/v) glycerol, 5 mM $CaCl_2$, 1 mM phenylmethanesulfonyl fluoride (PMSF), and 1 μM leupeptin, pepstatin A, and aprotinin. Cells were lysed by sonication in four sets of two minutes each. 0.5% CHAPS (w/v) was added to the total lysate and left to rock for 1 h on ice. Soluble fractions were then obtained by centrifugation in a Beckman J2-21 centrifuge at 20,000*g* at 4 °C for 60 min. Lysate was bound to HisPur Cobalt resin (Thermo Scientific) for 2 h with rocking at 4 °C. The Cobalt resin was washed with the following buffers at pH 7.5: (a) 50 mM Tris, 1 M NaCl, 5% Glycerol, and (b) 50 mM Tris, 300 mM NaCl, 20 mM imidazole. The bound protein was eluted with buffer containing 50 mM Tris, 300 mM NaCl, and 300 mM imidazole (pH 7.5). Proteins were then purified on a Superdex 75 (GE life sciences) size exclusion chromatography column with a buffer containing 50 mM Tris and 400 mM NaCl (pH 7.5). Purified proteins were buffer exchanged into 25 mM HEPES and 50 mM NaCl (pH 6.0) using Zeba Spin Desalting Column. Samples were analyzed by Sodium dodecyl sulfate–polyacrylamide gel electrophoresis (SDS–PAGE) gel for purity. Transformed BL21 cultures were grown to an optical density of 0.6 at 37 °C and induced with 0.5 mM isopropyl β-D1-thiogalactopyranoside (IPTG) for 4 h at 23 °C. Cells were lysed as described above and lysate bound to GST resin (Thermo Scientific). The resin was washed with a 50 mM Tris, 150 mM NaCl, pH 7.5 wash buffer and eluted with 50 mM Tris, 150 mM NaCl, 200 mM glutathione. A Zeba Spin Desalting Column was used to remove glutathione. Purified human kibra protein composed of the two N-terminal WW domains (a. a. 1–91) fused to a histidine tag was a gift from Dr. Afua Nyarko (Oregon State University, USA).

Liposome preparation. Liposomes were prepared as described previously [13,14]. Chloroform-dissolved lipids (80 mol% POPC and 20 mol% POPS) were mixed and dried under vacuum overnight to remove solvent. The dried lipids were then rehydrated in a 20 mM Tris, 100 mM NaCl, pH 7 solution to a concentration of 1 mM and extruded using a membrane with a 50 nm pore size. 1-palmitoyl-2-oleoyl-*sn*-glycero-3-phospho-L-serine (POPS), 1-palmitoyl-2-oleoyl-*sn*-glycero-3-phosphocholine (POPC) lipids, and extruder were purchased from Avanti Polar Lipids. For measurements using laudran, ∼1 mol% was dissolved with the POPC and POPS lipids and dried under vacuum. Laurdan was purchased from Sigma Aldrich.

Fluorescence measurements. Measurements were conducted using a QM-40 (Photon Technology International, Birmingham, NJ). The laurdan generalized polarization (GP) value was calculated using $GP = (I_{430} - I_{480})/(I_{430} + I_{480})$. I_{430} and I_{480} are emission intensities at 430 and 480 nm respectively [15]. Data were collected at a 1.0 nm step size with an integration time of 0.1 s. Each sample was measured multiple times to ensure that the system reached steady state. Sample buffer consisted of 20 mM Tris, 100 mM NaCl, pH 7.4. Fluorescence anisotropy measurements of GFP-linker constructs were conducted using an excitation of 460 nm and emission at 520 nm. Fluorescence anisotropy is defined as $A = I_{VV} - I_{VH}/I_{VV} + 2I_{VH}$.

Circular dichroism

Far UV circular dichroism (CD) measurements were recorded at 25 °C on a JASCO J-810 spectropolarimeter using a path length of 1 mm, and a bandwidth of 1.0 nm. Prior to data collection, the protein was dialyzed against 10 mM sodium phosphate (pH 7.5). The final concentration of the protein for CD analysis was 10 or 20 μM and reported CD data are the average of experimental repeats.

NMR measurements

The ^{15}N and ^{15}N/^{13}C isotopically labeled proteins were prepared in NMR buffer (pH 6.0), containing 25 mM MES, 50 mM NaCl, a protease inhibitor mixture (Roche Applied Science), 5% D2O, and 2,2-dimethylsilapentane-5-sulfonic acid for 1H chemical shift referencing, and were collected at a concentration of 100 μM. NMR spectra were collected at 283 K on an 800-MHz Bruker Avance IIIHD spectrometer equipped with a TCI cryoprobe. Backbone resonance assignments were determined from a set of [^{15}N, ^{1}H] BEST-TROSY based triple-resonance experiments (HNCA, HNCACB, HNCOCACB, HNCO, HNCACO) using pulse sequences from the standard Bruker library in Topspin 3.5.7. NMR spectra were processed with nmrPipe and analyzed with NMRViewJ [16,17]. All data were analyzed using a sine squared function, zero-filled to twice the size, Fourier transformed, and phased using nmrPipe. TALOS-N was used to calculate disorder propensity [18]. All 3D datasets were collected using non-uniform sampling (NUS) with 25% sparsity and a fully random sampling pattern. NUS data were reconstructed using SMILE and nmrPipe [16].

Sedimentation assay

Recombinant otoferlin or dysferlin protein was mixed with liposomes composed of 20 mol% POPS and 80 mol% POPC in buffer (20 mM Tris, pH 7.4, 150 mM NaCl). The mixture was incubated for 10 min at 23 °C and centrifuged at 65–90,000*g* for 45 min in a TA-100 ultracentrifuge (Beckmann Instruments). Supernatant and pelleted fractions were subsequently analyzed by SDS–PAGE.

Computational simulations

Molecular dynamics simulations were performed with the GROMACS package [19]. All systems were modeled with the coarse-grained SPICA force-field [20–22]. A custom patch from the SPICA developers (https://github.com/SPICA-group/gromacs-spica) was applied to GROMACS before compilation to enable the SPICA angle potential. The initial structure of the largely disordered linker domains was obtained using AlphaFold 2 (AF2) through a local ColabFold installation (version 1.5.5) which queries the (https://api.colabfold.com) server for the multiple sequence alignment [23,24]. The initial structure for the otoferlin C2A domain was obtained from the protein databank (PDBID: 3L9B). All-atom membrane patches with a composition of 75% POPC and 25% POPS were first built with the CHARMM-GUI webserver (https://www.charmm-gui.org/) [25,26]. Each membrane leaflet contained 220 lipids (165 POPC and 55 POPS), which resulted in a patch of approx. 120 × 120 Å to accommodate the extended linkers. A linker or C2A domain was then placed in the vicinity of the membrane patch (within 10 Å), but not directly in contact with the lipids during initial setup. A water layer approximately 100 Å thick was added to the system to allow ample space for the proteins to bind and unbind from the membrane. Sodium and chloride ions were added to neutralize the system and have concentration corresponding to 150 mM NaCl. After the complete system was built, the SPICA-tools (https://github.com/SPICA-group/spica-tools) were used to convert the all-atom system to the CG SPICA model [21,22]. Secondary and tertiary protein structural elements were maintained using and elastic network model with a force constant of 1.195 kcal/Å^2 and a cutoff of 9.0 Å. For dysferlin, the AF2 model predicts a short anti-parallel beta-sheet and loop structure at the N-terminus between residues 1 and 19. For isoforms 1 and 2, the AF2 model predicts a longer anti-parallel beta-sheet structure with residues 105–111 complementary H-bonding residues 121–127 at the C-terminus, which is preceded by an alpha-helical region between residues 82 and 100. For myoferlin, the AF2 model predicts a short alpha-helical region between residues 51 and 60.

Electrostatic interactions were computed using the particle-mesh Ewald method with a real space cutoff 1.5 nm and a Fourier grid spacing of 0.5 nm, while Van der Waals interactions were computed using 12–4 or 9–6 Lennard-Jones potentials with a cutoff of 1.5 nm. Newton's equations of motion were integrated with a leap-frog algorithm using a 20-fs time step. The temperature of the system was held constant at 37 °C using a velocity-rescaling algorithm with a time constant of 1 ps, and the pressure was held constant at 1 atm using a semi-isotropic stochastic cell-rescaling algorithm using a time constant of 5 ps [27]. Five independent replicas were run with different initial membrane configurations. Each replica was first energy minimized for 1,000 steps using a steepest descent algorithm, followed by a 100 ns membrane equilibration period where the protein was under harmonic position restraints using spring constants of 1,000 kJ/mol/nm^2. After equilibration, each replica was simulated without any restraints for 2 microseconds. Positions of all atoms were saved to the trajectory in 100 ps intervals. Trajectory analysis was performed with the

MDAnalysis python library and plots were generated with Matplotlib [28–30]. Graphical representations of the CG systems were created with NGLview.

Results

Ferlin C2A–C2B linkers encode putative membrane binding and SLiM sequences

To identify disordered regions within ferlin proteins, we analyzed the amino acid sequence of otoferlin, dysferlin, myoferlin, Fer1L5, and Fer1L6 using IPRED3 (Figure 1) [31]. Among several shorter predicted disordered regions we found two long disordered sequences within otoferlin that include the alternatively spliced C2A–C2B linker and a second sequence between C2D and C2F (Figure 1). Disorder within the C2A–C2B linker was also found for dysferlin, myoferlin, and to a lesser extent for Fer1L5 (Figure 1, arrow). Although lacking a C2A domain, Fer1L6 appears disordered at the N-terminus.

Multiple vertebrate ferlins including otoferlin undergo alternative splicing within the C2A–C2B linker [9–12]. Examination of the otoferlin cochlear (Q9ESF1, canonical isoform 1) and brain enriched (Q9ESF1-2, isoform 2) linker sequences reveal a disproportionate number of positively charged lysine and arginine residues, and few hydrophobic residues (Figure 2A). Isoform 2 encodes an additional sequence SKGREETKGGRDGEHK near the middle of the linker (Figure2A). Based on the fraction of negative and positively charged

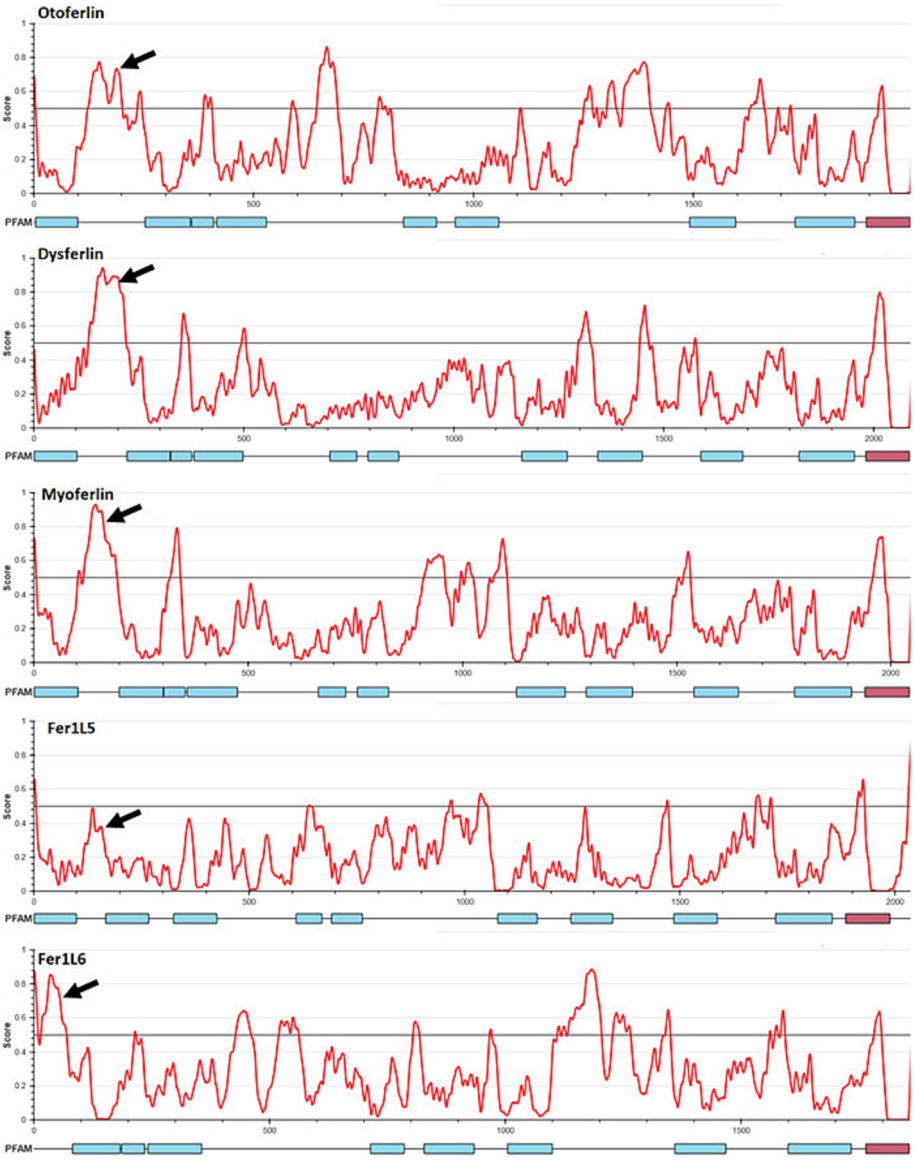

Figure 1. Output of IUPred3 for ferlin proteins otoferlin, dysferlin, myoferlin, Fer1L5, and Fer1L6. Arrow denotes the intrinsically disordered region at the N-terminus.

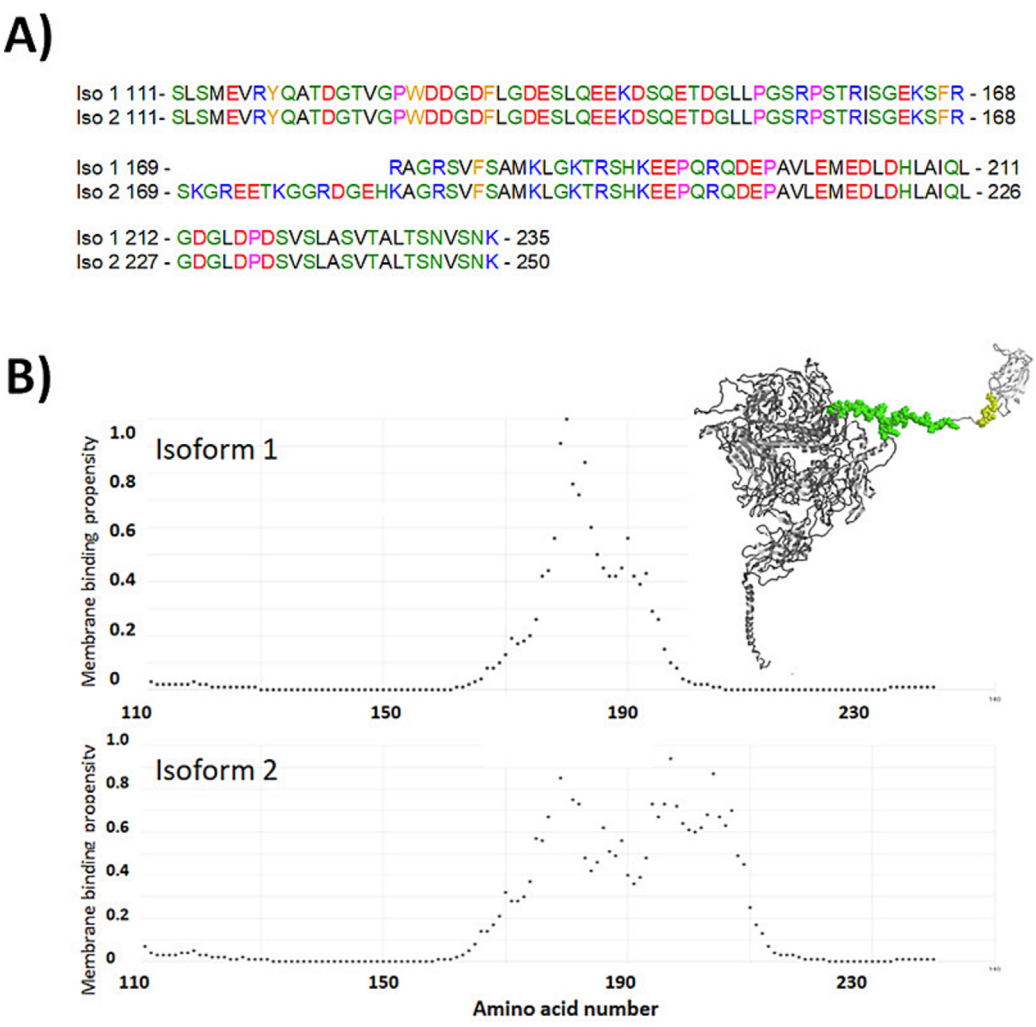

Figure 2. (A) Amino acid sequence alignment of C2A–C2B linker residues for otoferlin Q9ESF1-1 (isoform 1) and Q9ESF1-2 (isoform 2). (B) ReSMAP predicted membrane-binding propensities for otoferlin residues 110–240 for Uniprot Q9ESF1-1 (top panel) and Q9ESF1-2 (bottom panel). Inset displays the Alphfold predicted structure of otoferlin in which the dileucine motif is highlighted in yellow and the predicted membrane binding residues highlighted in green.

residues, both linker sequences reside in the Janus region of a Pappu diagram of states plot, suggesting context dependent conformations (Figure S1) [32]. Given the enrichment in positively charged residues within the linker isoforms we next assessed the potential of the linker sequences to interact with lipid membranes using Residue-Specific Membrane-Association Propensities of intrinsically disordered proteins (ReSMAP) [33]. Analysis of the linker using ReSMAP revealed a putative membrane binding sequence (a.a. 140–180) located in the middle of the linker region (Figure 2B). Charged residues compose approximately 35% of the 40 a.a. region identified by ReSMAP, with 20% of the sequence encoding for arginine and lysine. The additional lysine enriched sequence found within isoform 2 generates a second putative membrane binding sequence located proximal to the first binding region (Figure 2B). The first putative binding region display maxima at residues 168–170 which includes R168 and R169. The second putative binding region within isoform 2 peaks at R187. The identified binding regions appear to be conserved across species, ranging from mouse to zebrafish (Figure S2). Analysis of the remaining vertebrate ferlin C2A–C2B linkers suggest variability in their membrane binding properties (Figure S2). For dysferlin (O75923), a small putative binding sequence was found at the extreme C-terminus of the linker proximal to the adjacent C2B domain. Like otoferlin a known dysferlin splice variant adds additional residues within the C2A–C2B linker; however, this sequence was not identified by ReSMAP as interacting with membranes. Instead, the inserted residues include a short linear motif (SLiMs) sequence ETWSLL identified using Eukaryotic Linear Motif (ELM) as a putative acidic dileucine AP2 binding motif [34]. Further, curated spliced variants

of the human myoferlin C2A–C2B linker appear to alter the number of endocytic SLiMs, with the canonical sequence encoding for up to 6 SH2 and SH3 binding SLiMs, two of which are not found in the alternatively splice linker. We conclude that multiple vertebrate ferlins appear to encode a membrane binding sequence within the C2A–C2B linker, and alternative splicing of otoferlin increases the number of predicted membrane interacting sites while splice variation of the linker in dysferlin alters the number of putative SLiMs within the linker.

The C2A–C2B linker binds negatively charged membranes

Given the results of the ReSMAP prediction we sought to test whether the C2A–C2B linker binds membranes. We therefore conducted a liposome cosedimentation assay using a recombinant construct composed of otoferlin isoform 2 residues 141–209, encompassing the predicted membrane binding region. When mixed with liposomes composed of 100% 1-palmitoyl-2-oleoyl-*sn*-glycero-3-phosphocholine (POPC) the recombinant linker sedimented to small degree that did not reach statistical significance (Figure 3A). Given the linker sequence encodes for many charged and polar residues we also tested for linker-membrane interaction using liposomes composed of 20% 1-palmitoyl-2-oleoyl-*sn*-glycero-3-phospho-L-serine (POPS) and 80% POPC. In contrast to samples containing POPC liposomes, the linker construct cosedimented with negatively charged POPS/POPC liposome samples (Figure 3A, C). We also tested a separate construct composed of the N-terminal C2A domain and proximal linker (amino acids 1–140), which did not cosediment with liposomes regardless of POPS (Figure 3B, C). In addition, the N-terminal 1–140 construct failed to cosediment when added to liposome samples also containing the membrane binding 141–209 linker region, suggesting the membrane binding region does not recruit the N-terminal 1–140 segment. (Figure S3A). To determine if the shorter isoform 1 linker also bound membranes, we repeated the cosedimentation assay with a recombinant isoform 1 linker and found that like isoform 2, the shorter isoform 1 linker cosedimented with liposomes composed of 20% POPS (Figure 3C). Qualitatively we also found a recombinant dysferlin C2A–C2B linker composed of residues 101–217 also sedimented with POPS/POPC liposomes albeit to a lesser degree compared to otoferlin (Figure S3B).

The ferlin C2A–C2B linkers are predicted to be largely disordered [7]. To experimentally characterize the structure of the linker we collected circular dichroism (CD) measurements of residues of otoferlin isoform 2 as well as dysferlin (Figure 4). Consistent with a disordered structure we found that the linker spectra exhibited a minimum below

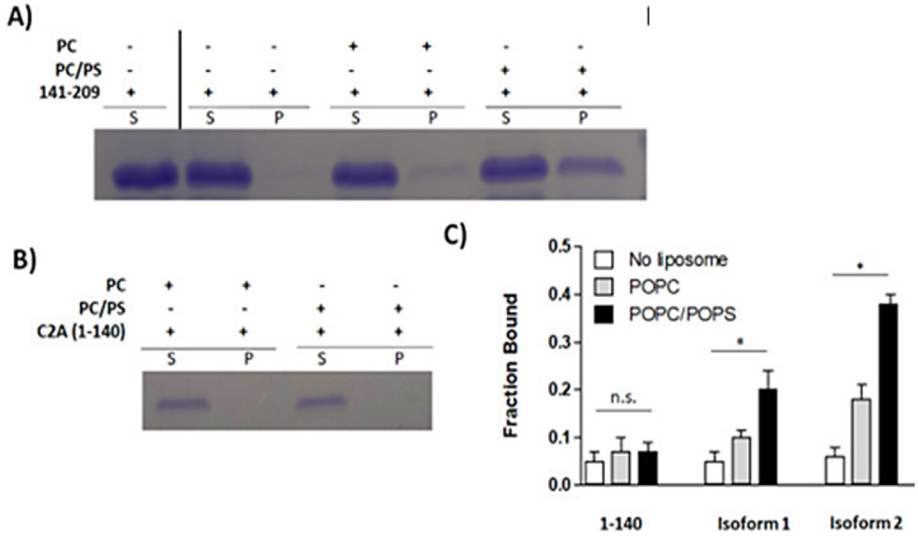

Figure 3. The otoferlin C2A–C2B linker cosediments with liposomes. (A) Representative image of Coomassie Blue stained SDS-PAGE gel showing cosedimentation samples for residues 141–209 mixed with POPC liposomes or 20% POPS/80% POPC liposomes. The first lane represents the protein input, with subsequent lanes for PC and POPC/POPS liposome samples. S denotes the supernatant and P the pellet. (B) The N-terminal residues 1–140 of otoferlin including the C2A domain do not cosediment with liposomes of either PC or PC/PS lipids. (C) Quantitation of the results of the liposome binding assay for 1–140, isoform 1, and isoform 2 linkers. The difference between POPC/POPS and no liposome conditions reached statistical significance (*t* test, * = $p < 0.001$). C2A–C2B sedimentation did not reach statistical significance for POPC conditions relative to no liposomes. Error bars represent ± standard deviation, n = 3. n.s. = not statistically significant.

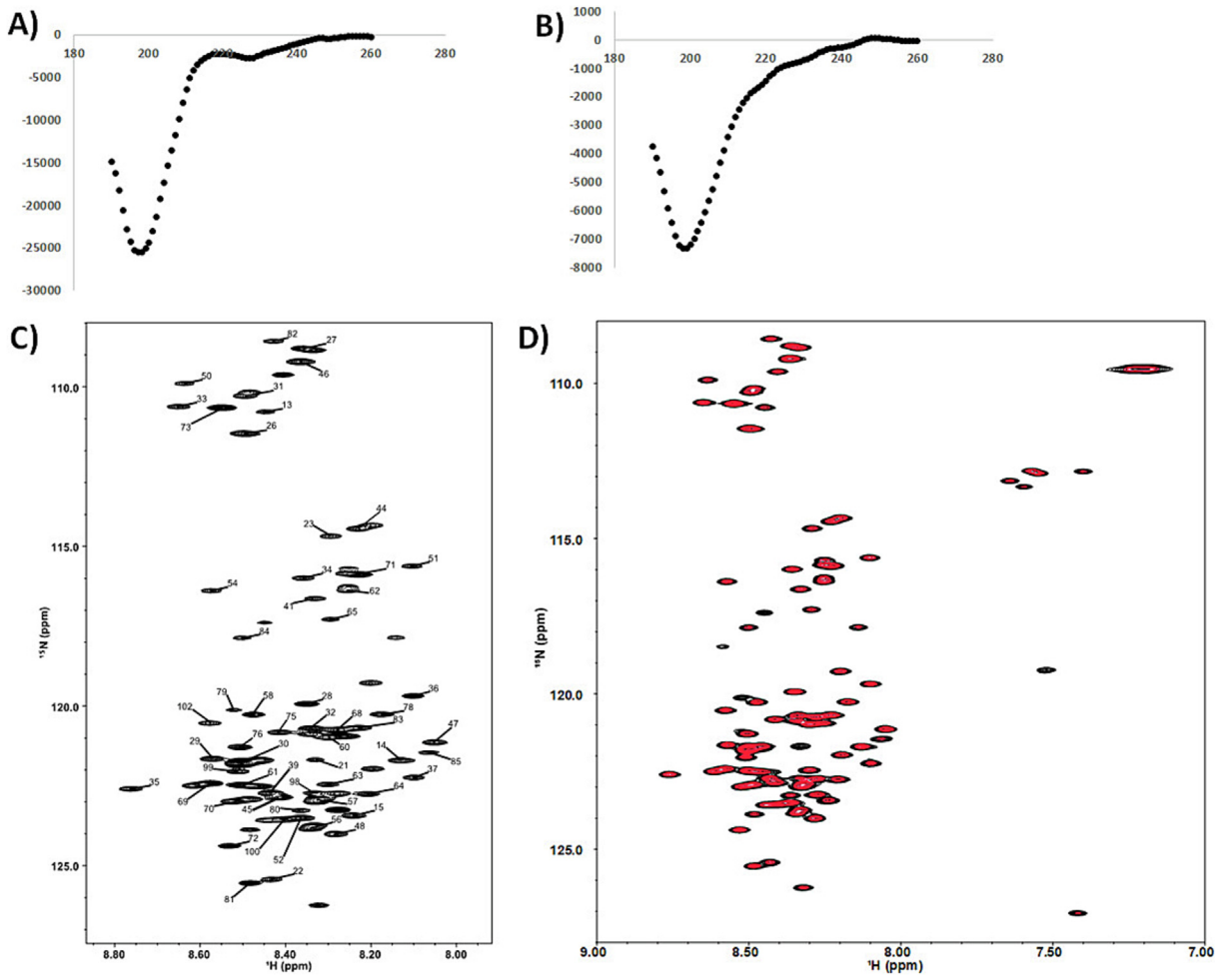

Figure 4. Circular dichroism spectra of otoferlin (A) and (B) dysferlin C2A–C2B linker. (C) ^{15}N–^{1}H spectra of otoferlin residues 141–209. (D) ^{15}N–^{1}H spectra of the linker in the presence of POPS/POPC liposomes. Decreased peak intensity for amino acids influenced by lipids are indicated in red.

200 nm and was absent of any positive CD signal (Figure 4A, B). Subsequently we used solution NMR to assign the resonances of C13, N15 isotopically labeled linker residues 141–209 of otoferlin and found the chemical shifts resided in a narrow range of values indicative of a disordered polypeptide, in agreement with the CD spectra (Figure 4C). Analysis using N-TALOS also indicated the linker is disordered (Figure S4). As a test for lipid interaction, we monitored changes in the chemical shift of N15 labeled 141–209 linker when mixed with POPC/POPS liposomes (Figure4D). The addition of liposomes to the sample reduced the intensity of resonance peaks for the N15 labeled recombinant linker, consistent with decreased degrees of freedom upon interaction with liposomes.

As an additional independent method of measuring membrane interaction, we monitored binding using laurdan-labeled liposomes. Laurdan is a solvatochromic membrane probe with an emission maximum that shifts upon protein absorption to the liposome surface [13,15,35,36]. When mixed with liposomes we found the linkers of both otoferlin isoforms shifted the laurdan emission in a dose-dependent manner (Figure 5). Best fits to a single-site model indicate lower affinity (K_d = 32 ± 4 μM, n = 3) for isoform1 relative to the longer splice isoform 2 (K_d = 14 ± 5 μM, n = 3). We also measured a construct composed of a.a. 1–209 encoding both the C2A domain and adjacent linker and found that the inclusion of the domain did not shift the titration curve significantly (*t*-test yields $p \approx 0.82$). This result agrees with our cosedimentation studies and suggest residues 1–140 including the C2A domain does not contribute to binding.

We conclude that the C2A domain and N-terminal linker residues (a.a. 1–140) do not interact with membranes, while residues 141–209 of the C2A–C2B linker contains a sequence that directly interacts with negatively charged lipids.

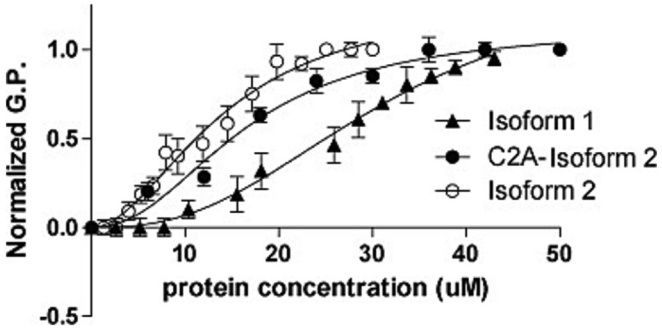

Figure 5. Both isoforms of the otoferlin C2A–C2B linker bind POPC/POPS liposomes. Titrations of isoform 1 linker, isoform 2 linker, and C2A-isoform 2 linker are plotted. The generalized polarization (GP) value was calculated using the emission intensity I at 430 and 480 nm, GP = $(I_{430} - I_{480})/(I_{430} + I_{480})$. Error bars represent S.D. n = 3.

The linker is the major contributor to the membrane binding activity of the C2A–C2B region of otoferlin

Previous studies have established that the C2A domain of otoferlin does not bind membranes while the C2B domain binds with low affinity [13]. To determine the contribution of the linker to membrane binding when coupled to the flanking C2A and C2B domains we tested a construct composed of both C2 domains and linker. When tested we found that the construct bound liposomes in a Ca^{2+} insensitive manner with a dissociation constant (K_d = 18 ± 1 μM ± 4 μM, n = 3) similar to the 141–209 linker construct (Figure 6). By contrast C2A did not shift the laurdan fluorescence emission up to the limit of the titration, in agreement with results of our cosedimentation assay. Titration of the C2B domain yielded changes in the laurdan fluorescence at high concentrations of the domain in agreement with previous studies which reported a low affinity interaction [13]. Thus the disordered interdomain linker is the major contributor to the membrane binding properties of the C2A–C2B N-terminus of otoferlin.

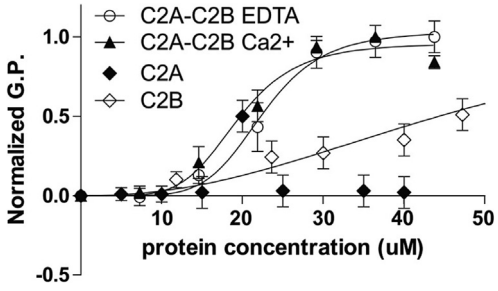

Figure 6. The otoferlin C2A–C2B linker contributes to the membrane binding activity of the N-terminal C2A–C2B region. Shown are titrations of single C2A domain which did not alter the fluorescence of the liposome embedded laurdan probe, as well as titrations of the C2B domain and C2A–C2B. Addition of otoferlin C2A–C2B shifts the G.P. value of laurdan independent of Ca^{2+}. The generalized polarization (GP) value was calculated using the emission intensity *I* at 430 and 480 nm, GP = $(I_{430} - I_{480})/(I_{430} + I_{480})$. Error bars represent S.D. n = 3.

Electrostatics mediate C2A–C2B linker-membrane interaction

The otoferlin C2A–C2B linker sequence is enriched in charged and polar residues including serine, arginine, glutamic acid, and aspartic acid. This enrichment suggests an electrostatic basis for the preferential interaction with charged lipids. To assess the influence of electrostatics, we tested for linker-liposome interaction under different salt concentrations (Figure 7). Compared to samples containing physiologically relevant NaCl concentrations (150 mM), measurements of samples containing 50 mM NaCl displayed greater binding sensitivity and an increase in the slope of the curve (Figure 7). Measurements of samples containing 400 mM "high" salt conditions had the opposite effect, leading to less sensitivity and a

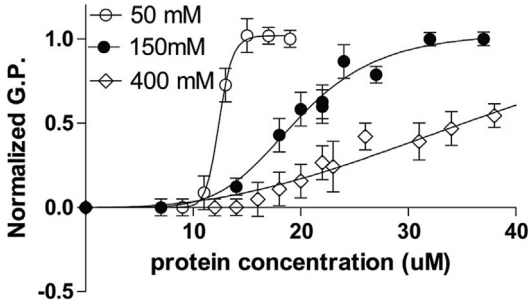

Figure 7. The interaction between the C2A–C2B linker and membranes is mediated by electrostatics, as monitored using laurdan-labeled liposomes. Titrations of the linker under 50 mM, 150 mM, or 400 mM NaCl are shown. The generalized polarization (GP) value was calculated using the emission intensity *I* at 430 and 480 nm, GP = $(I_{430} - I_{480})/(I_{430} + I_{480})$. Error bars represent S.D. n = 3.

gentler slope of the binding curve (Figure 7). These results agree with an electrostatic basis for linker-membrane interaction.

To gain additional insight into the observed interaction we performed coarse-grained (CG) simulations of both otoferlin linker isoforms in the presence of a POPS/POPC lipid membrane (Figure 8). For comparison we also included the otoferlin C2A domain, which does not bind membranes, and the dysferlin C2A–C2B linker. Relative to all-atom simulations, CG models offer a significant computational speedup due to the fewer number of interaction sites between molecules and faster configurational sampling due to the smoother free energy landscape [37]. The latter can often result in sampling three to ten times faster compared to all-atom systems [37,38]. The SPICA force-field has been shown to accurately reproduce structural, mechanical, and thermodynamic properties of lipid bilayers [21,22]. It also reproduces dimerization free energies of transmembrane helices and peptides in solution, membrane-protein interactions, and radius of gyration for intrinsically disordered proteins [21,39].

We first equilibrated the linker using an all-atom molecular dynamics simulation and subsequently applied the resulting energy-minimized structure in the SPICA coarse-grained simulation package. For all 5 replicates we found that over the span of the 2,000 nsec simulation time both otoferlin linkers increased the number of contacts with lipids in the membrane and associated with membranes using positively charged residues (Figure 8A, B). Analysis of the results revealed that isoform 1 displayed more instances of non-productive binding events, which we define as a

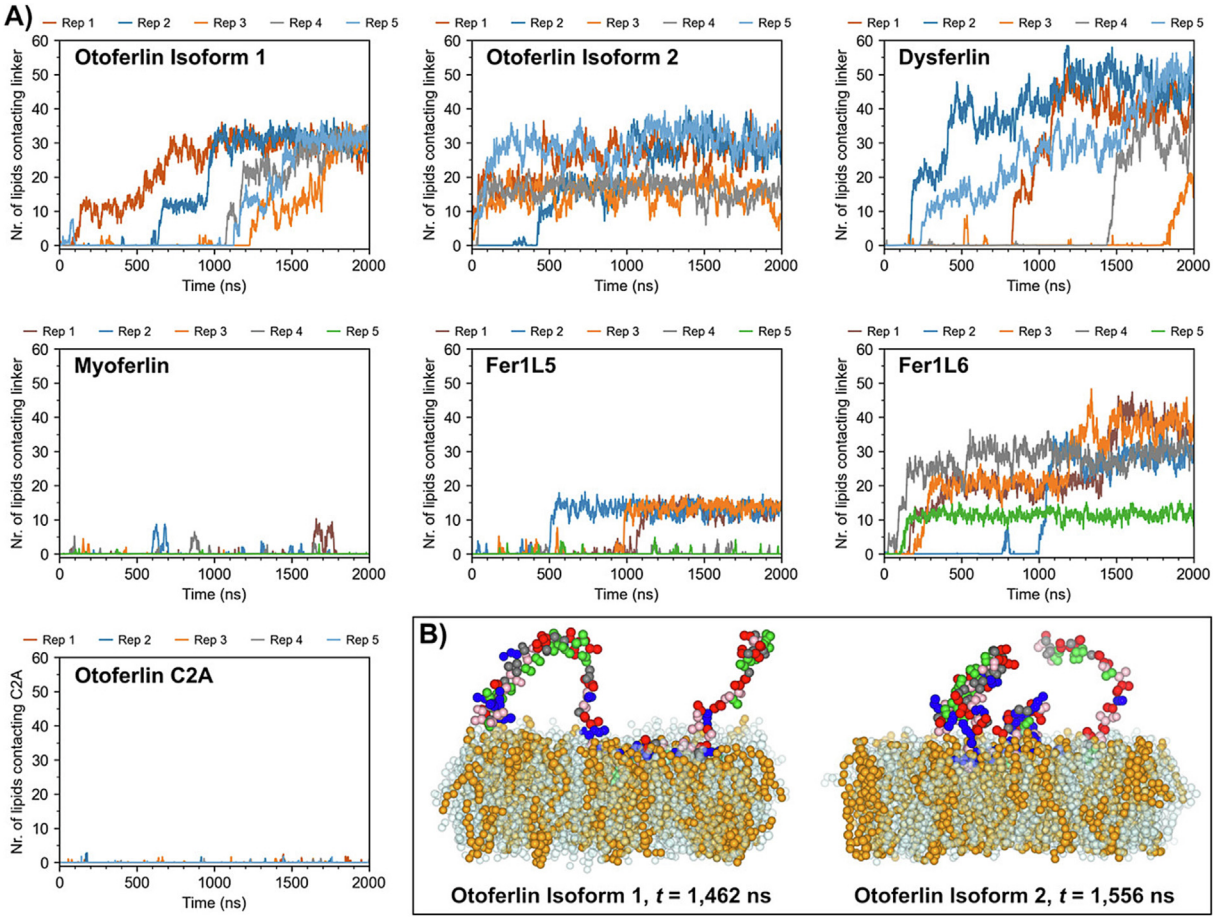

Figure 8. Coarse-grained MD simulations capture the binding interactions of ferlin C2A–C2B linkers with lipid membranes. (A) Number of lipids contacting the linker for POPC:POPS membranes for the vertebrate ferlins including both isoforms 1 and 2 of otoferlin, as well as the C2A of otoferlin. None of the 5 replicates for C2A displayed appreciable contacts. (B) Side (top) views of representative simulation trajectory frames of linkers interacting with the POPC/POPS membranes. Color legend: POPS: gold/orange, POPC: light blue/transparent, cationic residues (ARG, LYS, HIS): blue, anionic residues (GLU, ASP): red, polar (GLN, ASN, SER, THR): pink, hydrophobic (VAL, LEU, ILE, MET, PHE, TYR, TRP): green, other protein residues: gray. Regions with high frequency of anionic residues consistently avoid interacting with the membrane across all systems.

transient contact with at least one lipid but less than ten that does not progress to full binding (Table 1). The dysferlin linker displayed considerable variability between the 5 replicates, however in all simulations the linker bound membranes with a larger number of non-productive events than either otoferlin isoform 1 or 2 (Table 1). We conclude that the additional residues encoded by isoform 2 increase the number of successful contact events with the membrane.

We next extended our studies to examination of the other vertebrate ferlin linkers, which revealed membrane interaction for Fer1L6, and no significant interaction between the myoferlin C2A–C2B linker and membranes (Figure 8A). As an additional means to compare linker binding across family members we determined the average number of membrane contacts, POPC contacts, and POPS contacts for all linkers over t = 1800 n s – 2000 ns (Table 2). We found members could be broadly binned into linkers that formed few lipid contacts (myoferlin, Fer1L5) and linkers which made more extensive contacts (otoferlin, dysferlin, Fer1L6). Analysis of the number of lipid contacts formed with linker residues revealed a larger number contacts mediated by arginine rather than lysine for both otoferlin isoforms as well as dysferlin (Figure S5). We also found that the ratio of lipid contacts made with POPC and POPS (PC/PS) suggests dysferlin favors POPS less than the otoferlin linkers, which showed greater POPS contacts. However neither otoferlin isoform appeared to cluster POPC or POPS lipids as determined by comparison of the radial distribution function (Figure S6).

The dysferlin C2A–C2B linker interacts with endophilin

Analysis of the ferlin C2A–C2B linkers using the ELM database revealed multiple potential SLiMs within the dysferlin linker which are not found in the otoferlin linker, including motifs predicted to interact with SH3 and WW domains (Figure 9A). To determine whether the dysferlin linker interacts with proteins we measured the fluorescence anisotropy of polyhistidine-tagged eGFP-dysferlin (a.a. 124–219) or otoferlin (a.a. 100–249) linker constructs mixed with increasing concentrations of either the SH3- protein endophilin A1, or the WW-domain of the protein kibra (Figure S7). An increase in the measured anisotropy was observed upon the addition of endophilin to dysferlin but not otoferlin samples. Similarly, the addition of recombinant WW domain elicited an increase anisotropy upon mixing with dysferlin but not otoferlin linker proteins. Best fits to the dose–response curves with a single-site equation yield K_d values of 1.9 ± 0.01 μM and 7.7 ± 0.09 μM for endophilin and WW domain respectively (Figure 9B, C).

Table 1 Number of non-productive binding events observed over the 5 simulation replicates. Non-productive binding events are defined as contact with at least one lipid but less than ten that does not progress to full binding over the observed period.

Otoferlin C2A	64
Otoferlin Isoform 1	43
Otoferlin Isoform 2	1
Dysferlin	76
Myoferlin	87
Fer1l5	60
Fer1l6	11

Discussion

Ferlins are membrane trafficking proteins consisting of multiple Ca^{2+} sensitive domains interspersed between intrinsically disordered regions, including the linker between the C2A and C2B domains. Our comparison of vertebrate ferlin C2A–C2B sequences suggests a conservation of the presence of this linker among family members, but with divergent sequence compositions and activities. We found that the otoferlin C2A–C2B linker bound membranes with a moderate dissociation constant of 32 μM, and a brain-enriched isoform which inserts additional residues into the linker sequence shifts the K_d to approximately 14 μM. Although the determined affinities are modest, localization of the protein to the membrane will likely increase the local concentration and linker-membrane interaction. Binding was sensitive to phosphatidylserine and therefore the local surface density of negatively charged lipids may also contribute to linker affinity (Figures 2 and 3). The observed interaction was found to be sensitive to ionic strength as determined experimentally, suggesting an electrostatic basis for binding (Figure 6). Consistent with an electrostatic interaction, analysis of our computational results suggest the ferlin linkers form contacts with POPS preferentially over POPC (Table 2) and that the interaction is mediated by lysine and arginine residues (Figure S5). The otoferlin linker is hydrophilic with a calculated grand average hydropathy (GRAVY) of −1.0 for isoform 1 and −0.99 for isoform 2, and an enrichment of positively charged residues including 6 lysines and 7 arginines. Arginine-rich sequences are commonly found in many membrane binding and penetrating peptides where the charged guanidinium group interacts with charged components of the membrane. For comparison, the dysferlin linker has a calculated GRAVY of −0.68 suggesting a less hydrophilic (more hydrophobic) sequence relative to otoferlin. Results of coarse-grained simulations suggest the otoferlin linker makes a larger number of contacts

Table 2 Average number of protein-lipid contacts over each replica from 1800 ns to 2000 ns, for all linkers (95% confidence).

System	Average Nr. of lipid contacts	Ratio of PC:PS contacts
Otoferlin isoform 1	30.1 ± 1.47	2.29 ± 0.195
Otoferlin isoform 2	23.6 ± 10.5	2.64 ± 0.656
Dysferlin	35.5 ± 19.5	2.93 ± 0.446
Myoferlin	0	0
Fer1L5 (reps 1,2,3)	13.0 ± 2.15	2.64 ± 1.93
Fer1L6	29.5 ± 13.3	2.52 ± 0.285

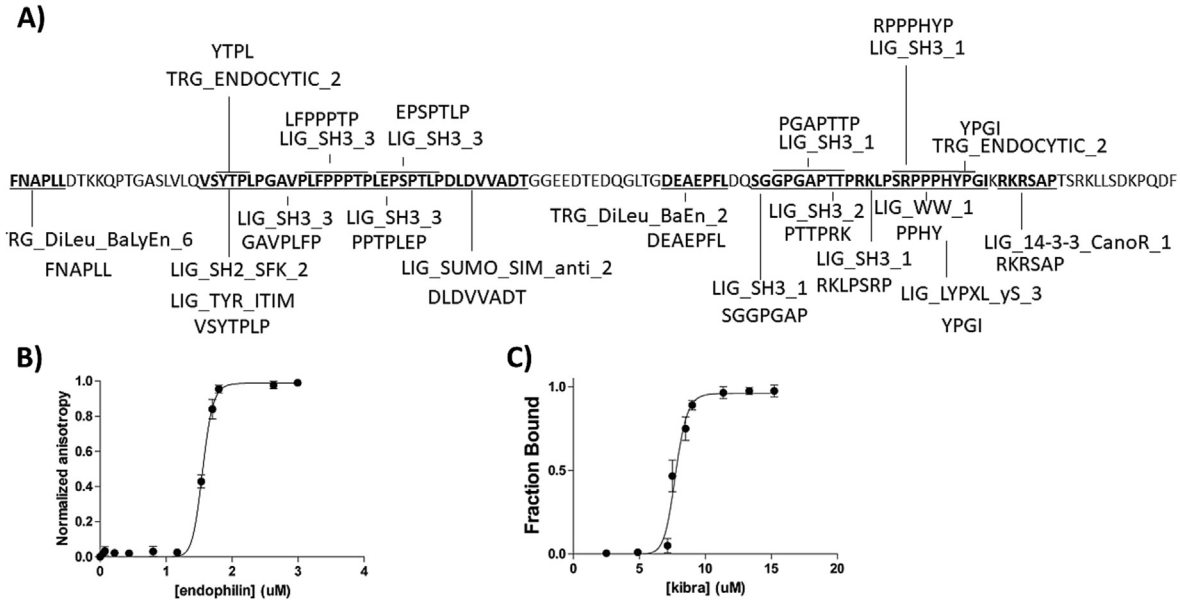

Figure 9. (A) Predicted SLiMs that interact with AP2, SH2, SH3, or WW domains residing within the dysferlin C2A–C2B (a.a. 101–219) and determined using The Eukaryotic Linear Motif database (ELM). SLiMs are underlined and annotated using the ELM classification. (B) Fraction endophilin A1 bound to eGFP-dysferlin C2A–C2B linker. Data was fitted using a single-site equation. K_d = 1.9 ± 0.01 μM, R^2 = 0.99 (C) Fraction kibra WW domain bound to eGFP-dysferlin C2A–C2B linker. Data was fitted using a single-site equation K_d = 7.7 ± 0.09 μM, R^2 = 0.98. Error bars indicate mean ± SD (n = 4). Error bars indicate mean ± SD (n = 4).

with POPS lipids compared to the dysferlin linker. In addition to otoferlin and dysferlin, we found Fer1L6 also made extensive membrane contacts which may be mediated by the large number of lysines within the linker, which represent approximately 14% of the linker sequence.

In addition to lipid membranes, the otoferlin C2A–C2B linker is reported to bind AP2 via a dileucine SLiM located several residues N-terminal from the membrane interacting region (Figure 2B, inset) [40]. Given the short distance between the dileucine motif and membrane binding region of the otoferlin linker we propose that otoferlin participates in vesicle recycling by placing the motif near the membrane for AP2 recruitment. Similarly, dileucine motifs are often found in the cytoplasmic tail of membrane proteins where the proximity of the motif to the membrane is proposed to promote AP2 membrane recruitment and activity. For example the cytoplasmic C-terminus of CD4 encodes a dileucine sequence proximal to the transmembrane domain which engages AP2 during endocytosis [41]. Several spacer residues found between the binding motif and the end of the transmembrane domain of CD4 are required for optimal AP2 binding, and a similar spacing requirement may account for the residues between the AP2 and membrane binding regions of otoferlin C2A–C2B (grey linker residues between yellow and green segments in Figure 2B inset). A previous study which focused on a shortened otoferlin splice isoform lacking the N-terminal 182 a.a. noted attenuated endocytosis and vesicle recycling compared to an isoform that included the N-terminus [10]. We speculate that loss of the linker region may contribute to the endo-

cytic deficiencies associated with the shortened otoferlin.

Like otoferlin, the dysferlin linker bound membranes, however the linker differs from otoferlin in the larger number and type of SLiMs, which include motifs predicted to interact with AP2, as well as SH3-, WW-, and SH2-domain proteins. Using endophilin A1 and kibra as representative SH3- and WW-domain proteins, we found that both bound dysferlin, but not the otoferlin linker as determined from anisotropy measurements. While endophilin is typically associated with endocytosis and the recruitment of dynamin, WW-domain proteins contribute to signal transduction processes and ubiquitination [42,43]. Cellular conditions where dysferlin may associate with these proteins remains to be determined however based on our results we conclude that the dysferlin linker acts as a platform for the recruitment of proteins with interaction modules. We speculate that the identity of the proteins occupying linker binding sites may depend on the specific subcellular location and conditions such as phosphorylation of the linker. By contrast the otoferlin linker appears to encode few SLiMs and may be optimized for a more specific function in vesicle replenishment. Given that multiple SLiMs are also predicted for the C2A–C2B linkers of myoferlin and Fer1L5, we suggest that protein recruitment may be a general function for this linker.

CRediT authorship contribution statement

Ethiene Kwok: Investigation, Formal analysis. **Patricia Khuu:** Investigation, Formal analysis. **Erin Huang:** Data curation. **Fakhria Saadat:** Data curation. **Elijah Urbaitel:** Data curation. **Jordan S. Indrawan:** Data curation. **Patrick Reardon:** Formal analysis. **Juan Vanegas:** Writing – original draft, Methodology, Investigation, Formal analysis. **Colin P. Johnson:** Writing – review & editing, Writing – original draft, Supervision, Methodology, Investigation, Funding acquisition, Formal analysis, Conceptualization.

Funding

This work was supported by the National Science Foundation MCB 2019386. The Oregon State University NMR Facility is supported in part by the National Institutes of Health, HEI Grant 1S10OD018518 and by M. J. Murdock Charitable Trust Grant 2014162.

DATA AVAILABILITY

Data will be made available on request.

DECLARATION OF COMPETING INTEREST

The authors declare that they have no known competing financial interests or personal relationships that could have appeared to influence the work reported in this paper.

Appendix A. Supplementary material

Supplementary material to this article can be found online at https://doi.org/10.1016/j.jmb.2025.169419.

Received 21 March 2025;
Accepted 1 September 2025;
Available online 4 September 2025

Keywords:
IDR;
linker;
membrane;
endocytosis;
disordered

† Contributed equally.

References

[1]. Huang, Y., Liu, Z., (2009). Kinetic advantage of intrinsically disordered proteins in coupled folding-binding process: a critical assessment of the 'fly-casting' mechanism. *J. Mol. Biol.* **393**, 1143–1159.

[2]. Sigrist, S.J., Haucke, V., (2023). Orchestrating vesicular and nonvesicular membrane dynamics by intrinsically disordered proteins. *EMBO Rep.* **24**

[3]. Roux, I. et al, (2006). Otoferlin, defective in a human deafness form, is essential for exocytosis at the auditory ribbon synapse. *Cell* **127**

[4]. Reisinger, E. et al, (2011). Probing the functional equivalence of otoferlin and synaptotagmin 1 in exocytosis. *J. Neurosci.* **31**

[5]. Abdullah, N., Padmanarayana, M., Marty, N.J., Johnson, C.P., (2014). Quantitation of the calcium and membrane binding properties of the C2 domains of dysferlin. *Biophys. J.* **106**, 382–389.

[6]. Padmanarayana, M. et al, (2014). Characterization of the lipid binding properties of otoferlin reveals specific interactions between PI(4,5)P2 and the C2C and C2F domains. *Biochemistry* **53**, 5023–5033.

[7]. Dominguez, M.J., McCord, J.J., Bryan Sutton, R., (2022). Redefining the architecture of ferlin proteins: insights into multi-domain protein structure and function. *PLoS One* **17**

[8]. Leclère, J.C., Dulon, D., (2023). Otoferlin as a multirole Ca^{2+} signaling protein: from inner ear synapses to cancer pathways. *Front. Cell. Neurosci.* **17** https://doi.org/10.3389/fncel.2023.1197611.

[9]. Yasunaga, I. et al, (2000). OTOF encodes multiple long and short isoforms: genetic evidence that the long ones underlie recessive deafness DFNB9. *Am. J. Hum. Genet.* **67**

[10]. Liu, H. et al, (2023). Cochlear transcript diversity and its role in auditory functions implied by an otoferlin short isoform. *Nature Commun.* **14**
[11]. Dwi Pramono, Z.A. et al, (2009). Identification and characterisation of human dysferlin transcript variants: implications for dysferlin mutational screening and isoforms. *Hum. Genet.*, 413–420.
[12]. Dwi Pramono, Z.A. et al, (2006). Identification and characterization of a novel human dysferlin transcript: dysferlin_v1. *Hum. Genet.*, 410–419.
[13]. Marty, N.J., Holman, C.L., Abdullah, N., Johnson, C.P., (2013). The C2 domains of otoferlin, dysferlin, and myoferlin alter the packing of lipid bilayers. *Biochemistry* **52**
[14]. Abdullah, N., Padmanarayana, M., Marty, N.J., Johnson, C.P., (2014). Quantitation of the calcium and membrane binding properties of the C2 domains of dysferlin. *Biophys. J.* **106**
[15]. Celli, A., Lee, C.Y.C., Gratton, E., (2007). Fluorescence microscopy to study pressure between lipids in giant unilamellar vesicles. *Methods Mol. Biol.* **400**, 333–339. https://doi.org/10.1007/978-1-59745-519-0_22.
[16]. Delaglio, F. et al, (1995). NMRPipe: a multidimensional spectral processing system based on UNIX pipes. *J. Biomol. NMR* **6**
[17]. Johnson, B.A., Blevins, R.A., (1994). NMR view: a computer program for the visualization and analysis of NMR data. *J. Biomol. NMR*, 603–614.
[18]. Shen, Y., Delaglio, F., Cornilescu, G., Bax, A., (2009). TALOS+: a hybrid method for predicting protein backbone torsion angles from NMR chemical shifts. *J. Biomol. NMR* **44**
[19]. Abraham, M.J. et al, (2015). Gromacs: High performance molecular simulations through multi-level parallelism from laptops to supercomputers. *SoftwareX* **1–2**, 19–25.
[20]. Seo, S., Shinoda, W., (2019). SPICA force field for lipid membranes: domain formation induced by cholesterol. *J. Chem. Theory Comput.* **15**, 762–774.
[21]. Kawamoto, S. et al, (2022). SPICA force field for proteins and peptides. *J. Chem. Theory Comput.* **18**, 3204–3217.
[22]. Yamada, T. et al, (2023). Improved protein model in SPICA force field. *J. Chem. Theory Comput.* **19**, 8967–8977.
[23]. Mirdita, M. et al, (2022). ColabFold: making protein folding accessible to all. *Nature Methods* **19**, 679–682.
[24]. Jumper, J. et al, (2021). Highly accurate protein structure prediction with AlphaFold. *Nature* **596**, 583–589.
[25]. Lee, J. et al, (2016). CHARMM-GUI input generator for NAMD, GROMACS, AMBER, OpenMM, and CHARMM/OpenMM simulations using the CHARMM36 additive force field. *J. Chem. Theory Comput.* **12**, 405–413.
[26]. Wu, E.L. et al, (2014). CHARMM-GUI membrane builder toward realistic biological membrane simulations. *J. Comput. Chem.* **35**, 1997–2004. https://doi.org/10.1002/jcc.23702.
[27]. Mattia Bernetti, G.B., (2020). Pressure control using stochastic cell rescaling. *J. Chem. Phys.* **153**
[28]. Michaud-Agrawal, N., Denning, E.J., Woolf, T.B., Beckstein, O., (2011). MDAnalysis: a toolkit for the analysis of molecular dynamics simulations. *J. Comput. Chem.* **32**, 2319–2327.
[29]. Matplotlib_a_2D_graphics_environment.
[30]. Nguyen, H., Case, D.A., Rose, A.S., (2018). NGLview-interactive molecular graphics for Jupyter notebooks. *Bioinformatics* **34**, 1241–1242.
[31]. Erdos, G., Pajkos, M., Dosztányi, Z., (2021). IUPred3: prediction of protein disorder enhanced with unambiguous experimental annotation and visualization of evolutionary conservation. *Nucleic Acids Res.* **49**, W297–W303.
[32]. Das, R.K., Pappu, R.V., (2013). Conformations of intrinsically disordered proteins are influenced by linear sequence distributions of oppositely charged residues. *PNAS* **110**, 13392–13397.
[33]. Qin, S., Hicks, A., Dey, S., Prasad, R., Zhou, H.X., (2022). ReSMAP: web server for predicting residue-specific membrane-association propensities of intrinsically disordered proteins. *Membranes (Basel)* **12**
[34]. Dinkel, H. et al, (2012). ELM – the database of eukaryotic linear motifs. *Nucleic Acids Res.* **40**
[35]. Orlikowska-Rzeznik, H., Krok, E., Chattopadhyay, M., Lester, A., Piatkowski, L., (2023). Laurdan discerns lipid membrane hydration and cholesterol content. *J. Phys. Chem. B* **127**, 3382–3391.
[36]. Yu, W., So, P.T., French, T., Gratton, E., (1996). Fluorescence generalized polarization of cell membranes: a two-photon scanning microscopy approach. *Biophys. J.* **70**
[37]. Seo, S., Shinoda, W., (2019). SPICA force field for lipid membranes: domain formation induced by cholesterol. *J. Chem. Theory Comput.* **15**
[38]. Yamada, T. et al, (2023). Improved protein model in SPICA force field. *J. Chem. Theory Comput.* **19**
[39]. Improved protein model in SPICA force field_enhanced reader.
[40]. Jung, S. et al, (2015). Disruption of adaptor protein 2μ (AP-2μ) in cochlear hair cells impairs vesicle reloading of synaptic release sites and hearing. *EMBO J.* **34**, 2686–2702.
[41]. Wyss, S. et al, (2001). The highly conserved C-terminal dileucine motif in the cytosolic domain of the human immunodeficiency virus type 1 envelope glycoprotein is critical for its association with the AP-1 clathrin adapter. *J. Virol.* **75**, 2982–2992.
[42]. Sundborger, A. et al, (2011). An endophilin-dynamin complex promotes budding of clathrin-coated vesicles during synaptic vesicle recycling. *J. Cell Sci.* **124**, 133–143.
[43]. Salah, Z., Alian, A., Aqeilan, R.I., (2012). WW domain-containing proteins: retrospectives and the future. *Front. Biosci.* **17**